Journal of Nuclear Materials 581 (2023) 154382

Contents lists available at ScienceDirect

Journal of Nuclear Materials

journal homepage: www.elsevier.com/locate/jnucmat

Surface modification of ITER-like mirrors after one hundred cleaning cycles using radio-frequency plasma

Fabien Sanchez[a,*], L. Marot[a], R. Steiner[a], D. Mathys[b], P. Hiret[a], K. Soni[a], R. Antunes[a], M. Kisiel[a], C. Romero-Muñiz[c], L. Moser[d], F. Le Guern[e], J.J. Piqueras Meseguer[e], E. Meyer[a]

[a] Department of Physics, University of Basel, Klingelbergstrasse 82, CH-4056, Basel, Switzerland
[b] Swiss Nanoscience Institute, University of Basel, Klingelbergstrasse 50/70, CH-4056, Basel, Switzerland
[c] Departamento de Física Aplicada I, Universidad de Sevilla, E-41012, Seville, Spain
[d] ITER Organisation, Route de Vinon-sur-Verdon, 13115 St Paul-lez-Durance, France
[e] F4E, c/Josep Pla 2, E-08019 Barcelona, Spain

ARTICLE INFO

Article history:
Received 14 November 2022
Revised 8 March 2023
Accepted 8 March 2023
Available online 30 March 2023

Keywords:
ITER
First mirrors
Plasma cleaning
Reflectivity
Blistering

ABSTRACT

In ITER, the metallic first mirrors (FMs) will undergo erosion due to their proximity to the fusion plasma and deposition of materials originated from the first walls (mainly beryllium). In-situ plasma cleaning is a promising technique to conserve the FMs optical properties by means of ion sputtering. In this work, the evolution of the optical properties of single-crystal (Sc) and nanocrystalline (Nc) molybdenum (Mo) and rhodium (Rh) mirrors were investigated up to 100 cycles of consecutive contamination and cleaning. Aluminum oxide (Al_2O_3) was used as contaminant to replace the toxic beryllium. The plasma cleaning was carried out using a capacitively coupled argon (Ar) plasma excited by a 60 MHz radio-frequency generator resulting in the formation of a self-bias applied on the mirrors of -280 V. The plasma potential being around 30 V, the Ar ion energy was about 310 eV. The optical properties of the mirrors were assessed using ex-situ reflectivity measurements. Moreover, the surface topography was characterized by means of scanning electron microscopy (SEM), focused ion beam (FIB) and roughness measurements using atomic force microscopy (AFM). ScMo and ScRh mirrors formerly exposed to 80 successful cleaning cycles using aluminum/tungsten (Al/W) deposits and air storage exhibit drastic changes in their optical properties after being subject to cleaning cycles using Al_2O_3 as contaminant. Additionally, freshly polished ScRh were exposed to identical cleaning cycles. All Sc mirrors exhibited pits induced by the polishing procedure using diamond paste in addition of mounds/wavy patterns. The carbon incorporated during the polishing process was demonstrated to be responsible for the pitting of the surface. The Nc mirrors preserved their initial reflectivities after up to 100 cycles. The surface topography was systematically characterized and an average erosion rate for NcRh mirrors of about 59 nm per cycle has been estimated from FIB cross-sections. The optical properties of the Nc mirrors showed a superiority in the present study in comparison to the Sc materials due to the influence of their polishing procedures.

1. Introduction

During ITER operation, optical diagnostic systems will be used to characterize the fusion plasma [1]. To ensure their reliability, a labyrinth or mirrors will guide the light from the fusion plasma towards detectors placed outside of the reactor [2]. The mirrors in close proximity to the fusion plasma, commonly known as first mirrors (FMs), are prone to erosion (particle fluxes due to charge-exchange neutrals) and deposition (beryllium, tungsten, their mixtures oxides) from the tokamak inner walls materials. Since contamination cannot be avoided, active mitigation techniques are indispensable. These techniques consist in removing the contaminant layer and also sputtering the mirrors' surface to remove implanted atoms. However, the sputtering should not degrade the mirrors' surface and ensure conservation of the pristine optical properties. Investigations on the influence of the discharge gas, ion energy, mirror material and the operating conditions (e.g., pressure) have been previously performed to find the optimal cleaning conditions for the various types of contaminants.

* Corresponding author.
E-mail address: fabien.sanchez@unibas.ch (F. Sanchez).

https://doi.org/10.1016/j.jnucmat.2023.154382

Since beryllium is toxic, previous work demonstrated the possibility for aluminium to be used as a surrogate for Be [3]. Although its stoichiometry in ITER conditions is unknown, beryllium will very likely be deposited as oxide. In other studies previously reported [4,5], Al_2O_3 was used as a surrogate. In order to eliminate the contaminants without affecting the optical properties of the FMs, several plasma cleaning methods such as pulsed DC discharge [6] or radio-frequency (RF) [7–10] have been investigated with molybdenum and rhodium mirrors [11–13], both in the form of single-crystals and nano-crystallines.

Previous works performed at the University of Basel showed the capability of removing aluminum and its oxide [4]. Argon, helium and deuterium (including mixtures) have been studied as process gases, with ion energies between 60 and 600 eV [14–17]. Other studies [14,15] highlight the capability to remove deposits with either Ar or He by tuning the ion energy. Results were obtained within magnetic field and tokamak, addressing the feasibility of plasma cleaning in ITER [4–9,12,13].

A previous work performed at the University of Basel demonstrated the efficient removal of Al/W deposits up to 34 deposition-cleaning cycles [18]. The optical properties of the ScRh, NcRh and ScMo were conserved after 34 cleaning cycles, using 60 MHz Ar cleaning plasmas. By increasing the number of cycles up to 80 using the same cleaning parameters and contaminants, the ability to preserve the mirrors reflectivity was confirmed [19].

This work aimed at studying the evolution of the optical properties and surface morphology of Mo and Rh mirrors up to 100 deposition-cleaning cycles. Al_2O_3 was used as contaminant and both single-crystalline and nano-crystalline forms of Mo and Rh were investigated. New results on freshly polished ScRh and ScMo, ScRh that had previously undergone deposition-removal using Al/W as contaminant [19], were obtained. In addition, the optical properties of thick-coated NcRh mirrors were investigated after extreme numbers of plasma cleaning cycles.

2. Experimental part

2.1. Selected mirrors

Commercial rhodium and molybdenum nanocrystalline and (100) single-crystal mirrors, with 22 mm diameter each, were selected for this study. The optical properties of these mirrors were evaluated up to 100 cycles of Al_2O_3 deposition and plasma cleaning. Nc mirrors originated from the same provider were coated by means of magnetron sputtering on stainless steel substrates with thicknesses comprised between 5.6 and 10.6 μm (Table 1). The magnetron sputtering of Rh films was extensively studied and described in our previous papers [20,21]. The exact procedure followed for these mirrors cannot be detailed due to confidentiality reasons. During the study, additional NcRh provided by a different manufacturer were tested. Their behaviour under Al_2O_3 cleaning cycles are detailed in the Supporting Information (SI). The ScMo and ScRh-1 mirrors were the same as those used in a previous study [19], in which they were exposed to 80 plasma cleaning cycles using Al/W as contaminant. Afterwards, these samples were stored in air for two years and were not re-polished prior to the new cycling campaign. The optical properties of the ScMo and the ScRh-1 prior to the Al_2O_3 campaign can be found in figure S1. In addition, the ScRh-2 was initially polished. The polishing procedure consisting of mechanical polishing by diamond suspensions of 6/3/1 and 0.25 μm followed by a chemical/mechanical polishing using an oxide powder (alumina or silica or ceria) of 0.05 μm particle size mixed with a chemical etchant.

2.2. Experimental procedure

All Nc and Sc samples were subjected to cycles of Al_2O_3 contamination followed by plasma cleaning. The mirrors were accommodated in one sample holder, which was installed in a high-vacuum chamber with a base pressure on the order of 10^{-5} Pa as described in figure 1 of reference [18].

The contamination of the mirrors was done by means of reactive magnetron sputtering. A rotating magnetron, operated with a RF power (13.56 MHz) of 100 W was used with an aluminum target. The use a pressure of 3 Pa and mixture of Ar (89%) and O_2 (11%) resulted in 20 nm thick Al_2O_3 on top of the Mo and Rh mirrors as determined by Focused Ion Beam (FIB, Helios NanoLab 650) cross-section analysis. The aluminum oxide layer deposited was analysed by X-ray Photoelectron Spectroscopy (XPS, electron spectrometer equipped with a Leybold EA10/100MCD and a non-monochromatized Mg Kα X-ray source; hν = 1253.6 eV) and showed a binding energy of 75.3 eV for the Al2p core level which is characteristic of an aluminum oxide [22]. The atomic concentration was calculated using Al2p and O1s core levels. The method followed revealed atomic concentrations of 43 at.% and 57 at.%, for Al and O respectively, which is close to a stoichiometric Al_2O_3.

A capacitively-coupled Ar plasma was used to physically sputter the surface of the contaminated mirrors. The argon plasma was generated using a 60 MHz generator. The asymmetry of the system between the chamber grounded wall and the electrode resulted in the development of a negative self-bias at the electrode of −280 V using a power of 80 W applied on the electrode. Moreover, the plasma is positively charged (in a range of 30 V [23]) which adds up to an ion energy of around 310 eV. The plasma was generated at 0.13 Pa which yielded an Ar^+ flux of 1.2×10^{19} m^{-2} s^{-1}, measured by a Retarding Field Energy Analyzer (RFEA). Cleaning times of 50 to 60 min were found to be sufficient to completely remove the Al_2O_3 layer (i.e. Al2p core level signal below the XPS detection limit).

The optical properties, surface roughness and topography of the mirrors were evaluated after a given number of cycles. The total and diffuse reflectivities in the range of 250–2500 nm were measured using a Varian Cary 5 spectrophotometer. The specular reflectivity was directly obtained by subtracting the diffuse reflectivity from the total reflectivity. The surface morphology was investigated using SEM (Hitachi S-4800) and a profilometer (KLA-Tencor Alpha-Step D-100) was used to evaluate the arithmetic

Table 1
Plasma cleaning parameters, film thicknesses and erosion rates of the mirrors used in this work. The ScMo and the ScRh-1 were previously exposed to 80 cleaning cycles using Al/W as contaminant. The NcRh-1, NcRh-2 and NcRh-3 mirrors were prepared by the same manufacturer.

	ScMo	ScRh-1	ScRh-2	NcRh-1	NcRh-2	NcRh-3
Initial thickness (μm)	Bulk	Bulk	Bulk	6.2	5.6	10.6
Cleaning duration (min)	60	60	50	60	50	50
Number of cycles	90	31	35	90	80	100
Final thickness (μm)	–	–	–	0.8	1.2	4.6
Fluence (10^{24} m^{-2})	3.9	1.3	1.3	3.9	2.9	3.6
Erosion rate (nm.cycle^{-1})	–	–	–	60	56	60

roughness R_a. The surface topography was analysed by means of atomic force microscopy (AFM) operated in tapping mode with a highly doped PPP-NCLR silicon cantilever from Nanosensors. The length, width and the thickness of the cantilever were 225 μm, 40 μm and 6 μm, respectively. The resonance frequency and the spring constant were equal to $f = 160$ kHz and $k = 28$ N m^{-1}. Intermittent contact measurement was performed with an oscillation amplitude of 10 nm, employing a 10–15 μm high tip with an apex better than 10 nm. The AFM images were analysed to determine each sample roughness, both as arithmetic average (R_a) and root mean square average (RMS), and to obtain a bidimensional map of the power spectral density (PSD). FIB was used to determine the erosion rates of the coated nanocrystalline mirrors. Regular XPS measurements of the samples were performed to ensure the complete removal of the Al_2O_3.

3. Results and discussion

3.1. Single-crystalline molybdenum mirror (ScMo)

Figure 1 displays the evolution of the total, diffuse and specular reflectivities of ScMo in the 250–2500 nm range, after various plasma cleaning cycles. Prior to the start of the cycles campaign, the reflectivity of the sample was observed to be significantly affected by the presence of a native oxide layer, developed over the course of two years. Therefore, an initial 50 min long Ar plasma cleaning was performed to recover the mirror's optical properties ("Before cycling" in Fig. 1). The following discussion refers to the values at $\lambda = 250$ nm and to the roughness measurements performed by aims of a profilometer unless stated otherwise. The total reflectivity of the ScMo was not significantly affected by the

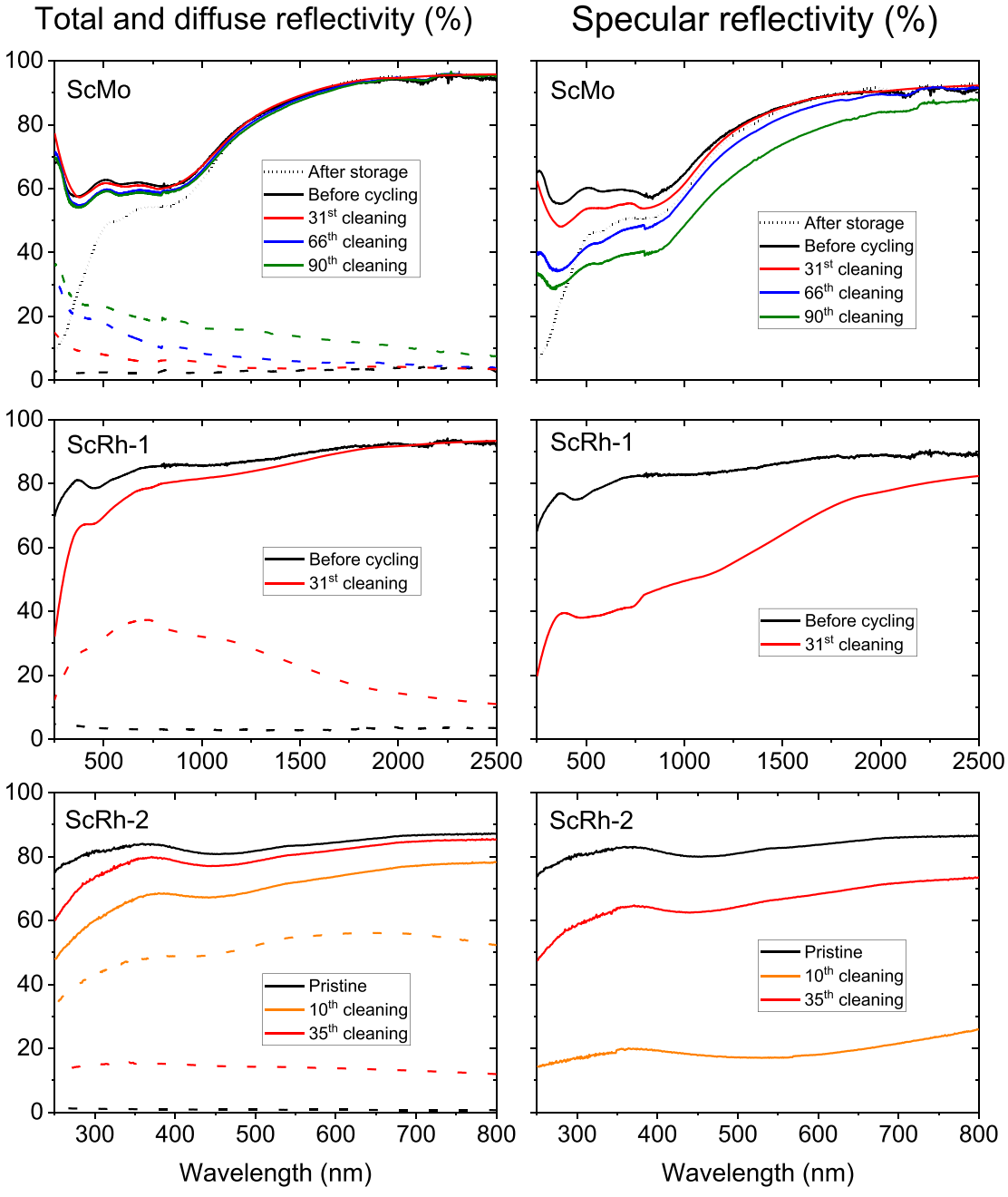

Fig. 1. Total, diffuse (dash lines) and specular reflectivity of the ScMo, the ScRh-1 and the ScRh-2 mirrors before and after various number of deposition-cleaning cycles.

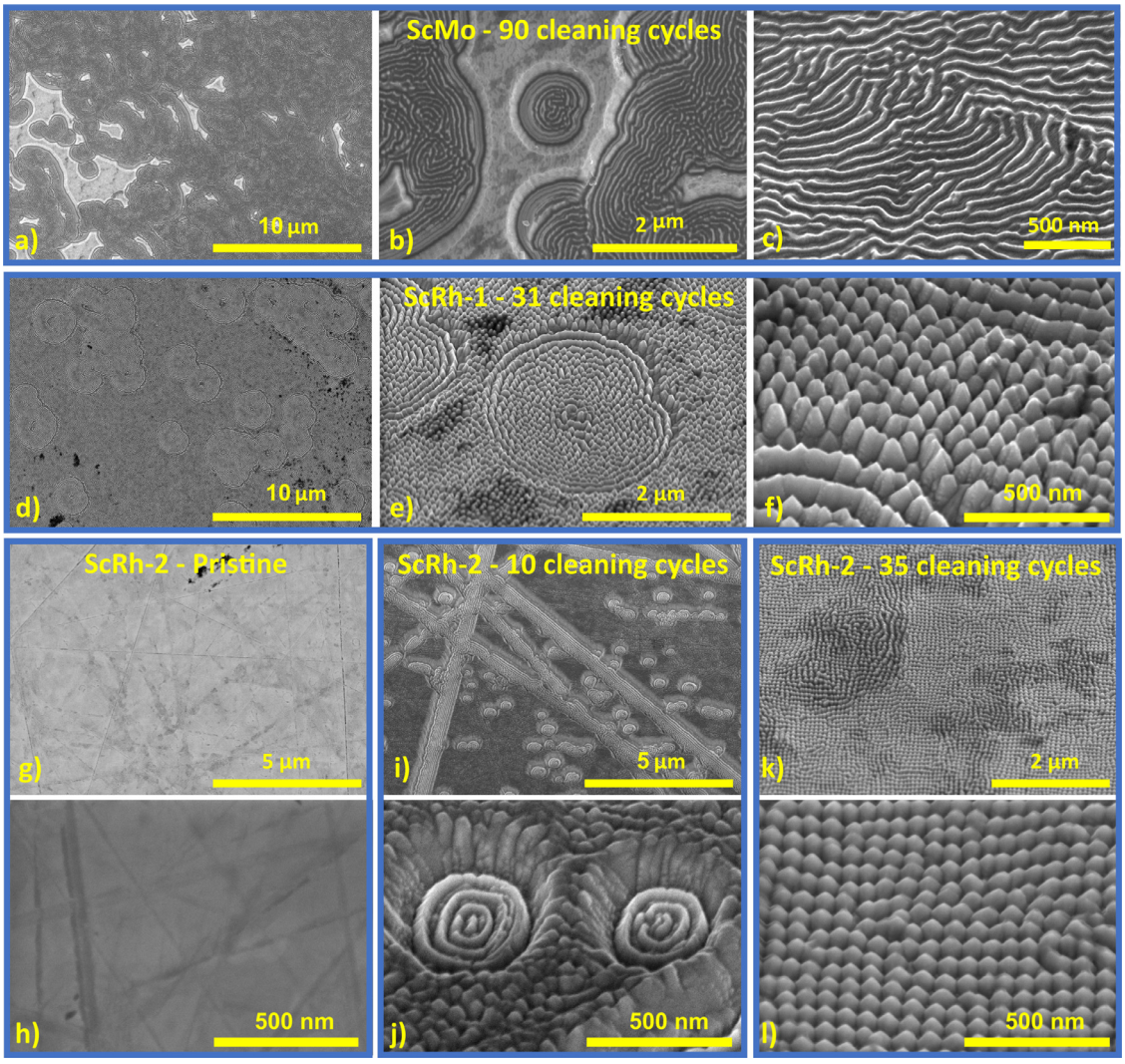

Fig. 2. Top and tilted (52°) views SEM images of a) the ScMo b) pits and c) wavy patterns after 90 cleaning cycles, d) the ScRh-1 e) pits and f) mounds structures, g), h) the ScRh-2 in its pristine state, i), j) after 10 cycles and k), l) after 35 cycles. Extra SEM images are figure S3 of the SI.

plasma-cleaning cycles. In contrast, the ScMo diffuse reflectivity is observed to increase from pristine to 90 cycles, from 3 to 36%, leading to a corresponding drop in the specular reflectivity, from 65 to 33%. The decrease in specular reflectivity is consistent with the increase in roughness, from 9 to 45 nm. Moreover, a wavy pattern (Fig. 2c)) and pits (Fig. 2c)) developed on the mirror' surface. The surface patterning of the ScMo will be addressed in the discussion part.

3.2. Single-crystalline rhodium mirror (ScRh)

The reflectivites measured on the ScRh-1 sample are displayed in Fig. 1. Contrary to ScMo, no oxide is formed on the rhodium surface and therefore there was no need to perform a pre-treatment using Ar plasma. The ScRh-1 sample was only subject to 31 cleaning cycles because of the significant deterioration of its optical properties as shown Fig. 1. As a result, the total reflectivity dropped from 70 to 36%. The diffuse reflectivity increased in the whole wavelength range resulting in a drop of the specular reflectivity from 65 to 20%. Moreover, the surface roughness evolved from 7 to 31 nm, which contrasts with the roughness of the ScMo obtained after 31 cycles: 8 nm. The topography of the ScRh-1 was analyzed using SEM (Fig. 2d), e) and f)) after 31 cleaning cycles. Two surface patterns can be recognized, a circular shape (Fig. 2e)) and mounds (Fig. 2f)). A similar analysis was performed on the polished ScRh-2. The SEM images of its surface exhibited polishing lines in its pristine state (Fig. 2g) and h)). After 10 cycles, the total reflectivity decreased from 75 to 48% and the diffuse reflectivity increased from to 1 to 34%, resulting in a decrease of the specular reflectivity from 74 to 14% (Fig. 1). In Fig. 2i) and j), an enhanced sputtering was observed at the polishing lines and circular patterns. Those pits showed an average diameter of 250 nm whereas the circular pattern on the ScRh-1 exhibited diameters of about 2500 nm after 35 cycles. After 35 cleaning cycles on the ScRh-2, the total reflectivity (Fig. 1) raised to 60% and the diffuse reflectivity dropped to 13%, yielding an increase of the specular reflectivity to 47%. At this step, the surface displayed only mounds (Fig. 2k) and j)) of 70 nm height and separated by 70 nm. The initial roughness of 4 nm increased to 13 nm and to 36 nm after 10 and 35 cycles, respectively. The pattern formations will be addressed in the discussion section.

3.3. Nano-crystalline rhodium mirrors (NcRh)

The optical properties of the three samples evolved similarly with the number of cleaning cycles (Fig. 3). Their average total reflectivities dropped from 72 to 63% after 80 to 100 cycles. For all three samples, the diffuse reflectivity did not exceed 10%, with

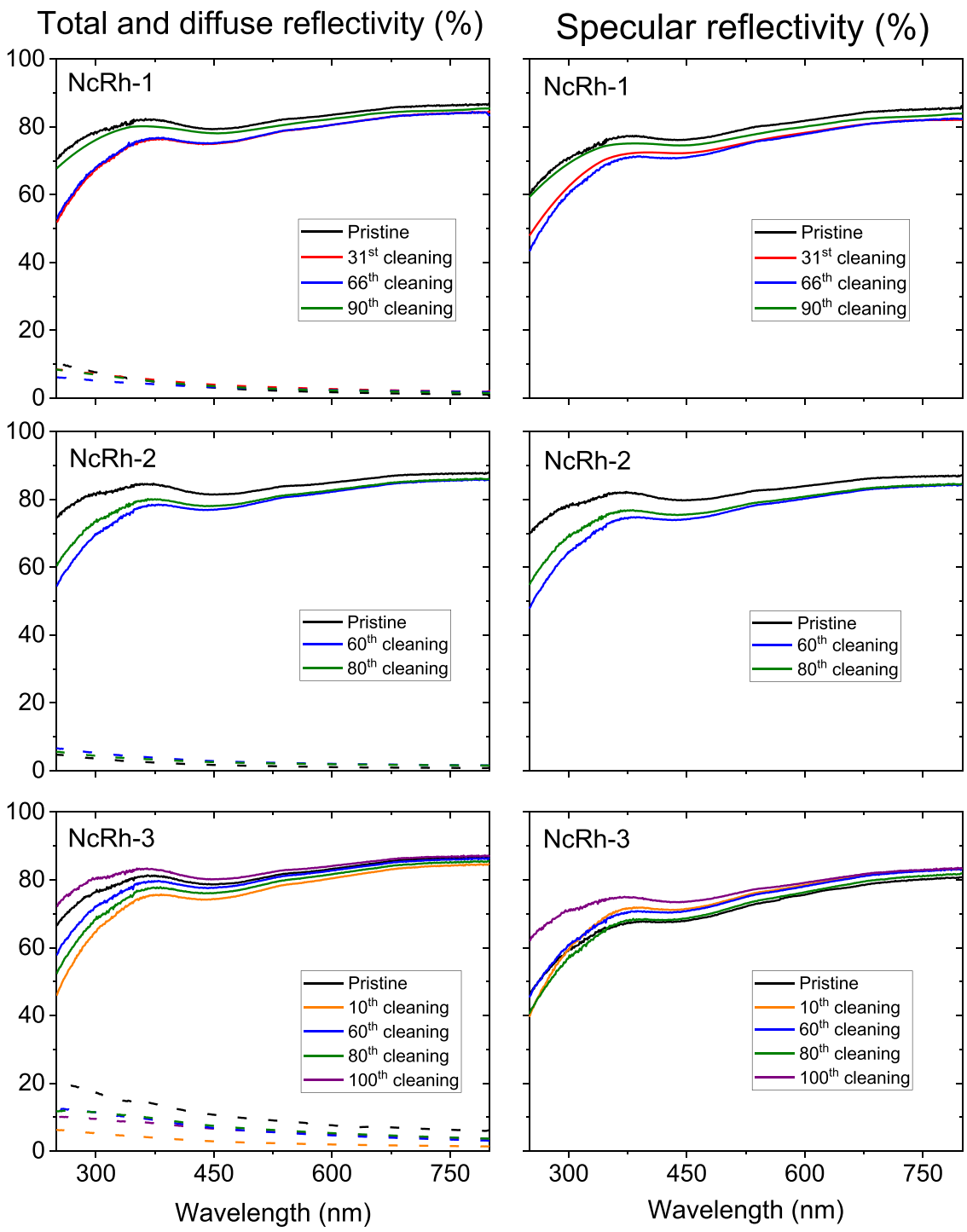

Fig. 3. Total, diffuse (dash lines) and specular reflectivity of 3 NcRh mirrors in pristine state and after up to 100 cleaning cycles. The coated thicknesses were of 6.2 μm, 5.6 μm, 10.6 μm for NcRh-1, NcRh-2 and NcRh-3, respectively.

the exception of the initial diffuse reflectivity of the pristine NcRh-3, which was equal to 20%. Before cycling, the roughnesses were equal to 5, 6 and 10 nm for NcRh-1, NcRh-2 and NcRh-3, respectively. After 10 cycles performed on the NcRh-3, a reduction of the diffuse reflectivity and roughness can be noticed. The NcRh-3 mirror had a 10.6 μm thick coating and exhibited defects on its surface, explaining the higher initial diffuse reflectivity.

After the cleaning cycles, the specular reflectivity of the NcRh mirrors decreased due to the lowering of the total reflectivity. Nevertheless, the specular reflectivity losses are quite negligible, making NcRh a promising material for ITER FMs. After 80 to 100 cleaning cycles, the roughness of the NcRh mirrors remained in the range of 5–7 nm, which is consistent with the evolution of the diffuse reflectivity. All three NcRh mirrors exhibited mounds with a periodicity of about 85 nm and 65 nm heights at the end of the deposition-cleaning campaign. Figure 4b) and c) show the SEM images taken for NcRh-1 after 90 cycles.

The NcRh mirrors conserved their initial roughness and specular reflectivity while these quantities increased for ScRh mirrors. Mound periodicity of both NcRh and ScRh mirrors were similar

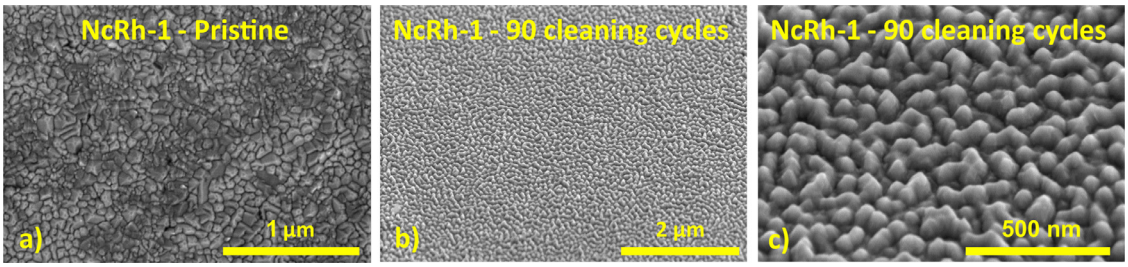

Fig. 4. Top and tilted (52°) views SEM images of NcRh-1 a) prior to plasma cleaning cycles and b), c) after 90 cycles of Al_2O_3 deposition-removal.

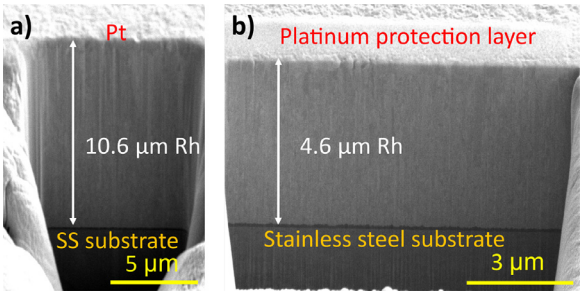

Fig. 5. FIB cross-sections of NcRh-3 mirror showing the coating thickness a) in the pristine state and b) after 100 cleaning cycles performed. A platinum layer was deposited prior to the FIB cross-sections to protect the surface of the mirror.

and about 70–90 nm. However, the ScRh developed 100 nm height mounds after 31 cycles (instead of 65 nm for the NcRh after 90 cycles). Moreover, no circular pattern was observed on the NcRh mirrors as presented in Fig. 4b) and c).

Using FIB, the thicknesses of the rhodium coatings of NcRh-1, NcRh-2 and NcRh-3 were measured at the end of the campaign. Figure 5 displays the cross-sections of NcRh-3 before and after 100 contamination-cleaning cycles. An average erosion rate of 59 nm cycle^{-1} was measured at the center of the NcRh mirrors. A higher erosion rate was observed along the edges of the mirrors. It is important to mention that ITER may use diverse gases, ion energies, fluences to clean the FMs from various types of contaminants. However, to cope with 100 cycles, a minimum initial coating thicknesses of about 7 µm can be estimated [1]. Additionally, end of cleaning indicators are foreseen in ITER [24], thus limiting the detrimental effect of the ion bombardment onto the FMs.

3.4. Topography analysis

The surface topography were analyzed through the use of a power spectral density (PSD) functions, which is the Fourier transform of the autocorrelation function that has been calculated from the surface profile applied on AFM images [25]. PSD analysis was performed on the ScRh-1 using the AFM image displayed in Fig. 6a). Due to a post-campaign repolishing of the ScRh-1, the AFM scan size was only 2 µm whereas 10 µm scan sizes were performed on the ScRh-2, NcRh-1 and the ScMo (Fig. 6b), c) and d)). Consistently with the SEM images (Fig. 2), the surfaces exhibited wavy structures, mounds and mounds after 90, 35 and 90 cleaning cycles, respectively. The AFM images (Fig. 6a)) of the ScRh-1 after 31 cycles displayed only the mound pattern. However, the corresponding SEM images (Fig. 2d), e) and f)) exhibited two patterns: the mounds and the pits. Thus, the statistical information obtained through PSD will correspond to the mound structures exclusively.

The two dimensional (2D) PSD shown in Fig. 6 are displayed using a Hann window and were obtained using the AFM images. The 2D PSD gives information about the relative contribution of all the possible surface spatial frequencies. The intensity distributions of the 2D PSD of the NcRh-1 and the ScRh-1 after the cleaning campaign do not exhibit a preferential orientations implying that the mounds are randomly distributed on the surface. Likewise, the 2D PSD of the ScMo present an isotropic intensity distribution. Instead, the ScRh-2 exhibited a cubic pattern (Fig. 6f)), which is a manifestation of the periodic arrangement of the mounds observed by SEM (Fig. 2k) and l)). The distance between the lobes of the 2D PSD and the center of the image are characteristic of the surface periodicity and were analyzed further with one dimensional (1D) PSD. Additionally, a second lobe order can be observed visible on the edges of the images (Fig. 6f)).

The 1D PSD represents the surface height squared (roughness power) per spatial frequency. It was calculated from the integration of the 2D PSD signal over x or y direction followed by an averaging of the obtained signals. Figure 7a) displays in a log-log plot the resulting 1D PSD profiles computed from AFM images. The 1D PSD were plotted as a function of the spatial frequency ν which is directly inverse proportional to the wavelength λ in the real space. PSD curves present generally the same characteristic shape, consisting of a at response in the lower part of the spatial frequency spectrum and a power-law dependence with the spatial frequency in the upper part the spectrum corresponding to the highly correlated region.

In Fig. 7a), the ScMo profile exhibited existence a plateau for spatial frequencies below 0.3 µm^{-1}. This trend is characteristic of a K-correlation model [26]. However, this model was not fitting the PSD profile. Thus, all the profiles correspond to a linear decrease (for ν above 0.3 µm^{-1}) of the PSD characteristic of a power-law dependence. As observed in dash lines in Fig. 7a), the profiles were fitted using a fractal model which is defined as an inverse power-law [27,28]:

$$PSD = \frac{K}{\nu^{\gamma}} \quad (1)$$

The fractal model is function of the spectral length K and the slope of the logarithmic plot γ. The 1D PSD signal can be analyzed through abnormal signal increase (above the trend described by the fractal model) providing the periodic surface arrangements and the slope value γ that can be correlated to the roughness.

Through the increase in the PSD intensity off the fractal model trend, surface arrangements can be determined. After 90 cleaning cycles performed on the ScMo, a linear decrease of the 1D PSD intensity with the increase of ν (above $\nu \approx 0.3$ µm^{-1}) is observed. Due to their random orientations of the surface pattern, no abnormal increase of the PSD intensity is observed and thus, the average distance between the “waves” of the pattern cannot be extracted. After 35 cleaning cycles performed on the ScRh-2, a signal increase is observed at around $\nu = 11.6$ µm^{-1} which corresponds to 86 nm in the real space. The distance between the mounds were found to be of about 70 nm measured by SEM (Fig. 2k) and l)) which is close to 86 nm. This peak was also observed on the 2D PSD through the presence of the lobes (Fig. 6f)). Additionally, a low intensity peak is observed at the end of the 1D PSD profile at around

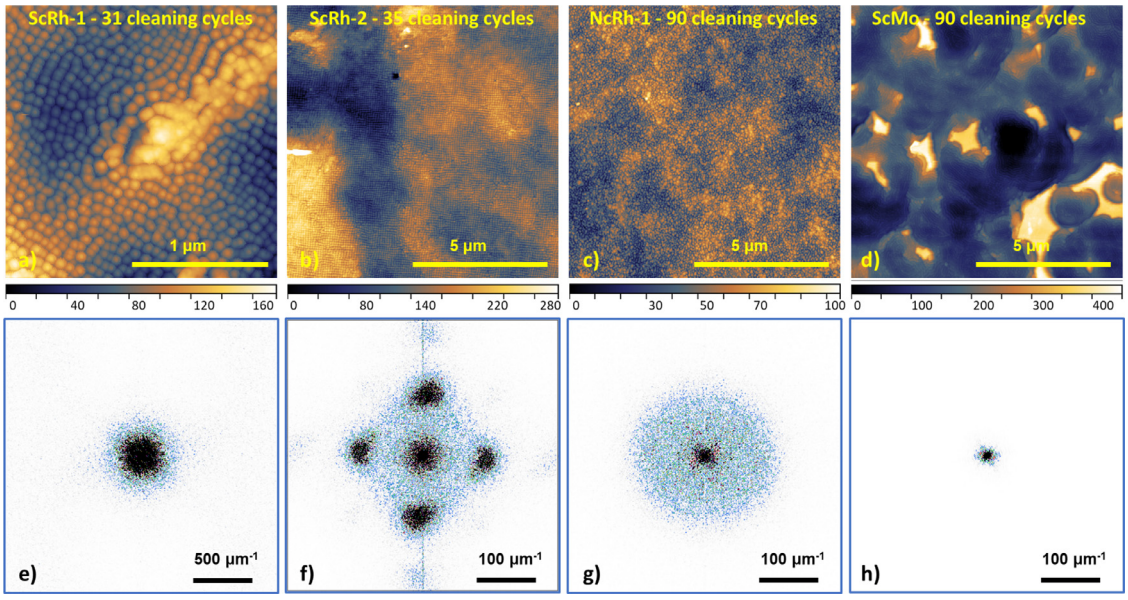

Fig. 6. AFM images of a) ScRh-1, b) ScRh-2, c) NcRh-1 and d) ScMo mirrors after 31, 35, 90 and 90 cleaning cycles, respectively. Images e) to h) are 2D PSD obtained with a radial Hann window of each AFM image.

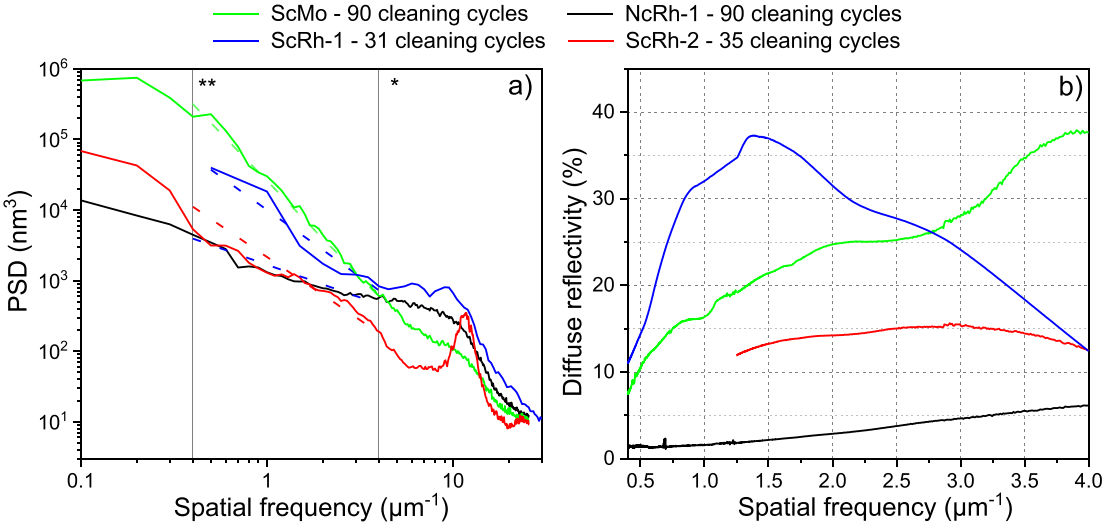

Fig. 7. a) is power-spectra obtained using an FFT after applying a Hann window to the full topography of the ScMo, ScRh-1, ScRh-2 and the NcRh-1 after 90, 31, 35 and 90 cleaning cycles performed. In dash, are the fitting of the curve for the spatial frequency range displayed using the inverse power law model. b) the diffuse reflectivity of the mirrors mentioned previously.

$\nu = 23\ \mu m^{-1}$ which corresponds to the second lobes of the 2D Hann window (Fig. 6f)). For both ScRh-1 and NcRh-1, the linear decrease in intensity of the 1D PSD is interrupted above around $\nu = 4.8\ \mu m^{-1}$. In the range of $\nu = 5\ \mu m^{-1}$ and $\nu = 14\ \mu m^{-1}$, a PSD intensity increase is observed. Those ν values correspond to mound distances comprised between 208 and 70 nm which include the average mound distance obtained through the analysis of the SEM images (Figs. 2f) and 4c)).

Additionally, the spectral length K and the slope γ were determined in the spatial frequency range displayed by the dashed line (Fig. 7a)) and reported in Table 2. The vertical lines marked with * and ** in Fig. 7a) correspond to the spatial frequency range in which the diffuse reflectivity was measured (250–2500 nm). In Fig. 7b), the diffuse reflectivity of the mirrors are displayed in spatial frequency values. The following discussion will only refer to the spatial frequency range previously mentioned. Firstly, all the 1D PSD profiles follows the power-law dependence. It indicates that no specific periodic arrangement inducing light scattering and increase of the diffuse reflectivity. Secondly, rises in diffuse reflectivity often corresponds to an increase in surface roughness (Bennett's law [29]) and the γ values are proportional to the roughness [30]. The NcRh-1 mirror after 90 cleaning cycles presented a γ value of 0.93 which is lower than the other mirrors and corresponds to the lowest diffuse reflectivity and roughness (measured by profilometer and AFM). The ScRh-2 and ScRh-1 exhibited γ values of 1.79 and 1.89 after 35 and 31 cleaning cycles, respectively. Even though the γ values are comparable, the diffuse reflectivity for the two mirrors were different. The ScRh-1 displayed a maximum of diffuse reflectivity at 37%, whereas for the ScRh-2 was only 15%. The roughness of the two samples measured with the profilometer and with AFM are comparable and higher than the ones measured for the NcRh-1. For the ScMo mirror, the γ is 2.72

Table 2
Surface roughness characteristics and the coefficients of the fractal model used to fit the 1D PSD for the NcRh-1, ScRh-2, ScRh-1 and the ScMo mirrors after being subject to 90, 35, 31 and 90 cycles, respectively.

	NcRh-1	ScRh-2	ScRh-1	ScMo
Roughness R_a (nm) - profilometer	7	36	31	45
Roughness R_a (nm) - AFM	9	14	20	40
Roughness RMS (nm) - AFM	12	18	25	57
K factor ($nm^{3-\gamma}$)	3.49×10^{9}	3.06×10^{15}	2.13×10^{16}	8.46×10^{22}
γ coefficient	0.93	1.79	1.89	2.72

and the diffuse reflectivity is the highest at 2 μm^{-1} (250 nm). The roughness values ranged between 40 and 57 nm which remained higher than the other mirrors.

From this analysis, the γ values determined using a fractal model can be linked with the mirror's diffuse reflectivities, except for ScRh-1, which showed a higher diffuse in regards to its γ value. However, the γ values are in line with the AFM roughness values (Table 2). It is worth mentioning that only the mound pattern was observed in the AFM images for the ScRh-1 and ScRh-2 (Fig. 6a) and b)). It indicates that the circular patterns were not contributing to the PSD intensities and therefore the differences observed in the diffuse reflectivity for those two mirrors could be due to the presence of the pit pattern observed on the ScRh-1. Moreover, the optical properties of the ScRh-2 (Fig. 1) after 10 cleaning cycles exhibited a degradation mainly through its diffuse reflectivity increase. After 35 cycles, partial recovery of its optical properties were observed simultaneously with the circular pattern removal.

4. Discussion

The discussion section aims at describing the mechanisms leading to the formation of the patterning observed on the mirrors during the cleaning campaign. A section will be conducted on the formation of the wavy structures and the mounds observed for the ScMo and the ScRh/NcRh, respectively. Afterwards, the pits observed on the Sc materials will be assessed.

4.1. Wavy pattern and mounds formation

The surface of the Sc materials exhibited patterning after the cyclic process due to the Ar ion bombardment. During the cycles, the surface temperatures of the mirrors were comprised between 298 and 500 K, the heat being generated by the irradiation (measured using a retractable thermoelement). On Fig. 2c), a wavy structure was observed on the ScMo mirror after 90 cleaning cycles while the rhodium specimens exhibited mounds as displayed in Fig. 2f), k) and l). In order to pattern surfaces, the material, the incident ion beam characteristics (mainly ion energy, incidence angle α and fluence) are key parameters. Wavy structures are commonly encountered on samples that were subjected to ion bombardment at oblique incidence [31] while in our experiments the Ar ions impinged the surface at normal angles. The nanopatterning of a metallic surface due to ion bombardment is a complex phenomenon. Nevertheless, shadowing is found to be the main mechanism. In the specific case of non-normal incidence ion bombardment, geometrical effects can induce the formation of local surface deflection. The curvature of the surface shadows the incident beam leading to the formation of sinusoidal wave-like patterns [32,33]. The development of wavy/mound pattern is enhanced by the dependence of the sputtering yield on the local surface curvature [31] as described by the Bradley-Harper theory. Nonetheless, nanodots were formed by Tan et al. using 1 keV Ar ions on InP(100) [34] and by Ziberi et al. using 1.8 keV Ar ions on Si [35] both at normal incidence. Moreover, Molle et al. [36] reported the formation of various nanostructures by bombarding face-centered cubic (110) metal surfaces at normal incidence with Xe ions at energies of few hundreds eV. During the sputtering process, a competition between kinetic and thermodynamic processes can lead to ripples, rhomboidal pyramids or rectangular ripples state as discussed in [37]. Studies done at the University of Genova [36,38] reported a surface patterning on ScRh(110) after Xe ion bombardment at 450 K. Within the range of 220 eV to 2500 eV, the ion mean energy demonstrated a major role on the Rh surface morphology. In our contributions, the ScRh-1 and the ScRh-2 mirrors displayed similar patterns induced by an argon ion bombardment having 310 eV ion energy (after 31 cycles and 35 cycles respectively). Similarly to ScRh, the ScMo displayed wavy surface structures after 90 cycles (Fig. 2c)) being formed by the ion bombardment.

4.2. Pits formation

4.2.1. Influence of the polishing process

The formation of the so-called "Beilby layer" has been reported to occur upon polishing of samples. Gorodetsky et al. [39] reported a Beilby layer thickness of 10–20 nm for polycrystalline (Pc) Mo specimens. Additionally, a 3–5 μm thick layer is formed below the amorphous Beilby layer, having a different structure from the rest of the metal. This 3–5 μm thick layer is a highly deformed layer with nanoscale crystallites that is gradually transforming into an undisturbed bulk [40]. During the polishing process, abrasive particles are embedded in the treated surface and leave deep holes filled with carbon, which lead to the introduction of micron and submicron diameter diamond powders in the material [41]. Diamond abrasive turned into particles of graphitized carbon. Its content was measured in the surface layer within a thickness of 1.5 μm [40]. Similarly, our Sc materials were mechanically polished using diamond pastes of 6/3/1 and 0.25 μm followed by a chemical/mechanical polishing using an oxide powder (alumina or silica or ceria) of 0.05 μm particle size mixed with a chemical etchant (Fig. 8a)). In our study, both ScMo and ScRh-1 were previously polished and subject to 80 cleaning cycles using Al/W [18,19]. It implies that the Beilby layer was already removed before starting the campaign with Al_2O_3. Additionally, the completeness of 80 Al/W cycles involve an estimated total removal of 1.7 and 2.3 μm for ScMo and ScRh-1, respectively. The previous removed thicknesses were estimated using the eroded thickness of a NcRh during the Al/W cleaning campaign and the sputtering yield of Mo. The sputtering yields of Mo and Rh being equal to 0.367 and 0.733 atoms/ion when bombarded by 310 eV Ar ions. However, the deformed layer ($\sim$ 3-5 μm) induced upon polishing may be thicker than the eroded thicknesses ($\sim$ 2 μm), providing residual carbon (Fig. 8g)). The ScRh-2 was polished and not subject to cleaning cycles prior to the cleaning campaign. As previously described, carbon from the polishing procedure is present in all the Sc mirrors. However, the carbon amount is expected to be lower for the ScMo and the ScRh-1 in comparison to the ScRh-2 due to the preceding cleaning campaign.

In order to confirm the presence of carbon in the materials' depth after polishing, additional ScRh were polished by

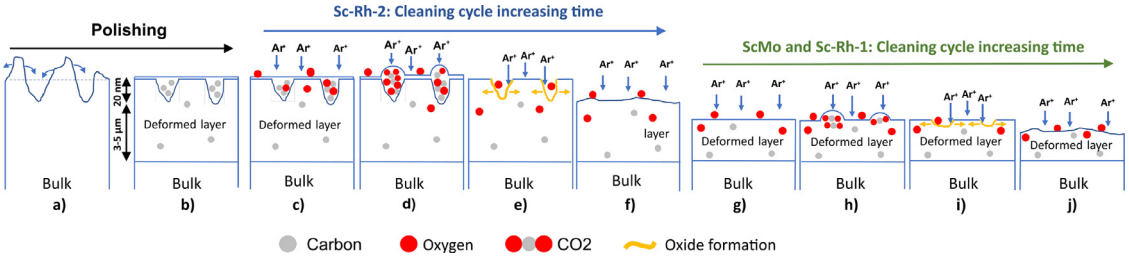

Fig. 8. Schematic of the a), b) polishing process and the mechanisms inducing surface morphology changes for a) to f) ScRh-2 and for g) to j) ScMo and ScRh-1.

Matech company (ScRh-3 and ScRh-4). The C amount of the ScRh-3 was quantified as a function of the depth using XPS and 2.5 keV Ar ions etching without breaking the vacuum. Around 3 at. % of carbon was measured at least till 0.65 µm in depth. Beyond 1.65 µm, no carbon was detected. These results are in line with Gorodetsky et al. publications [40] reporting the introduction of carbon in the metal bodies after the polishing process.

4.2.2. Blistering effects

Additionally to the carbon incorporated in the Sc mirrors, oxygen was introduced in the chamber during the coating procedure. Few minutes prior each Al_2O_3 deposition step, a Ar and O_2 plasma was generated in the chamber to homogenize the magnetron target. During this step and the ensuing Al_2O_3 deposition, the temperature of the sample was about 373 K. Moreover, upon Ar ion bombardment, the Al_2O_3 layer may follow an ion mixing leading to possible oxidation and oxygen diffusion on/in the surface, especially on the defects observed on the pristine surfaces (Fig. 2g) and h)) as described by Gorodetsky et al. [41] (Fig. 8c).

In literature, blistering effects have been reported on molybdenum surfaces bombarded by hydrogen, deuterium and/or helium gases [42]. Gorodetsky et al. [39] showed an enhanced blistering induced by small additions of O_2 or N_2 into 70–120 eV D_2^+. The bubble formation was accelerated, thus facilitating the blistering. Moreover, a surface oxide formation could prohibit remission of gas molecules into the gas phase and accelerate the blister nucleation and growth. More than the material composition, the crystalline orientation influences the blistering processes. It was reported that ScRh oriented [100] and [110] were prone to blistering but not the [111] direction [43]. The ScRh and ScMo mirrors used in this work were both exposed to oxygen and oriented [100] which is a preferential orientation to form blisters [43].

Gorodetsky et al. [40] reported the effects of cleaning of an Al layer (10–40 nm thick) on top of a ScMo using D_2-N_2 ions. Pits up to 50–100 nm deep and 50 to 500 nm width appeared. These pits were explained by the incorporation of diamond particles into the metal body upon polishing. During the cycling process, we hypothesis that oxygen diffusion induced the formation of gas bubbles and/or recombined with carbon to form CO or CO_2, thus causing blistering (Fig. 8h)). The mechanical deformed layer inhibited the nucleation of pores and hence increased the diffusion path and the oxidation rate (Fig. 8g)) [44]. The circular pit patterns observed on ScMo (Fig. 2b)), ScRh-1 (Fig. 2d) and e)) and on ScRh-2 (Fig. 2j)) are the results of such process. For the ScRh-2, the diffusion of oxygen in both the Beilby and deformed layers will occur (Fig. 8c)). Oxygen coalesces and bonds to carbon, leading to the formation of blisters (Fig. 8d)). Blisters burst under Ar bombardment due to local heating, leaving open linear grooves (Fig. 8e)) as observed on the ScRh-2 (Fig. 2i)) [45]. Linear polishing lines were revealed after removing the Beilby layer and thus grooves were formed similarly to pits on these defects [45]. As previously mentioned, the ScRh-1 and the ScMo were previously subject to 80 Al/W cleaning cycles. Thus, the Beilby layer was removed prior to the Al_2O_3 campaign and the linear grooves were not observed (Fig. 2a) and d)). The carbon amount is also expected to be higher in the ScRh-2 in comparison to the ScMo and the ScRh-1 due to the absence of Al/W pre-cycling. Consequently, deeper pits were observed on the ScRh-2 when compared to the ScRh-1 due to the presumed higher amount of resulting products (CO and CO_2) leading to blisters.

4.2.3. Influence of the oxide sputtering yields

In order to understand the development of the pits structures, investigations were done on the oxide sputtering yields in comparison to their pure metallic states. Usually, metal oxides have a reduced sputtering coefficient compared to their metallic surfaces. However, some refractory metals such as tungsten or molybdenum display the opposite behavior and the oxides sputter more rapidly than their bare metal counterparts, as experimentally observed [46]. This is due to the abnormally high sublimation enthalpy of the pure metal. According to the Sigmund's theory for sputtering [47], we can predict this behavior comparing the atomization enthalpy of the oxide with the sublimation enthalpy of the metal. Under this framework, we can expect that Rh and Mo oxides have higher sputtering rates than their pure metallic states, as shown by our thermodynamic calculations detailed in the SI.

Thus, the sidewalls of the grooves may be oxidized (Fig. 8e) and i)) and sputtered more quickly due to the difference of sputtering yield [48]. Moreover, the incidence angle of the ions coming to the sidewalls of the circular patterns and grooves would be close to grazing incidence, which is known to increase the sputtering yield [49]. By increasing further the ion fluence, the sidewalls of the pits (and the grooves in the case of the ScRh-2) extended and merged (Fig. 8f) and j)) as observed in Fig. 2i) and j) until their extinction (Fig. 2k) and l)).

4.2.4. Carbon influence on the pitting process

To validate our assumption, to new ScRh-3 and the ScRh-4 mirrors were polished the same way as the ScRh-1 and the ScRh-2 (diamond paste). Five cleaning cycles were performed on those mirrors starting with a ScRh-4 in its pristine state and with a ScRh-3 previously etched of 1.65 µm in depth. The latter was eroded prior to the cleaning cycles in order to remove the 2 to 6 at.% of C incorporated in the material depth during the polishing process (table. S3). As expected, pits and linear grooves developed on the freshly polished mirror (ScRh-4) however the ScRh-3 only exhibited mounds on its surface (fig. S3). The removal of the carbon content prior to the cycling process inhibited the pitting process confirming further the importance of the polishing process.

Additionally, the total, diffuse and specular reflectivity were measured for the ScRh-3 and the ScRh-4 (fig. S5). The diffuse reflectivity of the ScRh-4 after 5 cycles increased similarly to the ScRh-1 and ScRh-2 after 31 and 10 cycles, respectively. The ScRh-3 did not presented pits on its surface due to the surface etching procedure. Consequently, the diffuse reflectivity of the latter remained around 10% which is close to the one of the ScRh-2 after 35 cycles. These is consistent with the SEM observations of Fig. 2i), j) k) l) and S6.

5. Conclusions

Cycles of contamination and plasma cleaning have been carried out on single-crystal and nanocrystalline Rh and Mo mirrors. Ar plasmas with an ion energy of 310 eV showed the capability to sputter the 20 nm-thick Al_2O_3 contamination layers after 50–60 min exposure time. ScMo and ScRh-1 mirrors were previously exposed to 80 Al/W cleaning cycles and air storage. An additional plasma cleaning was performed on ScMo prior to the Al_2O_3 contamination-removal cycles in order to remove its native oxide layer. After the plasma cleaning campaign, Sc mirrors exhibited a degradation of their reflectivities in comparison to their initial states. Moreover, cleaning cycles were conducted on a freshly polished ScRh mirror showing similar results as non-polished ones with the degradation of their optical properties. In all the cases, wavy structures were formed on ScMo and mounds on ScRh after cleaning cycles due to the Ar irradiation. Additionally, pits developed on the surfaces of all the mirrors as well as linear grooves.

The following pits formation process were proposed: i) the polishing was performed using diamond paste, which leads to the accumulation of carbon in the deformed region down to a few μm, as demonstrated in the previous section, ii) the oxygen present in the chamber during the coating phase and Ar bombardment, possibly leads to ion mixing followed by oxidation and oxygen diffusion on/in the surface, especially at the defects, revealed after the removal of the Beilby layer; the extra dislocations in the deformed layer also increased the diffusion path and the oxidation rate, iii) the diffused oxygen might form gas bubbles and/or recombine with carbon to form CO or CO_2, iv) blisters burst upon Ar^+ bombardment resulting in pit structures. With the increase of the number of cycles, pits appeared on the surface and merged. It may be explained by a faster oxidation of the sidewalls of the pits, the possible higher sputtering yields of the oxides for these materials. When increasing the fluence, the pits completely merged and could not be observed any longer.

In order to link the topography of the mirrors with their optical reflectivity, a fractal model was used to fit the PSD profiles computed from AFM images. The γ values were extracted from the model and compared to the mirrors diffuse reflectivities. Larger roughness and diffuse reflectivity of the mirrors correspond to higher γ values. Only ScRh-1, previously exposed to 80 Al/W deposition-removal cycles showed, a higher diffuse. However, the AFM images used for the analysis do not display circular pattern. Moreover, the circular pattern appeared on the ScRh-2 after 10 cycles and the diffuse reflectivity increased to around 40% in the visible. After 35 cleaning cycles, the circular pattern were not observed and the diffuse reflectivity of this mirrors went down to around 16%.

During this campaign, three NcRh mirrors prepared by means of magnetron sputtering were tested. In contrast to the Sc mirrors, NcRh were not subject to a polishing step, which explains the absence of pits/grooves. The specular reflectivities of all the NcRh mirrors exhibited a decrease of around 18% at $\lambda = 250$ nm which is acceptable for ITER requirements.

These results suggest that NcRh mirrors can withstand at least 100 contamination-cleaning cycles, without significant deterioration of their optical properties. The set of cleaning parameters used in this work led to an average erosion rate of 59 nm per cycle for all the NcRh mirrors.

6. Outlooks

For ITER purposes, the NcRh exhibited a limited degradation of their optical properties. Nevertheless, the Sc mirrors remain one promising material for the FMs units regarding the overall possible contaminants in ITER. It implies the needs for mitigation strategies in order to counter the pit formation and the loss of their optical properties. Those pits were formed due to the polishing process performed using diamond paste and oxygen exposure. The formation of pits onto the FMs after only few cleaning cycles would completely compromise the optical diagnostic systems. In order to palliate the pit formation, the following strategies are suggested:

- Conservation of the polishing procedure using diamond paste and apply a former surface etching step of few μm thickness
- Change the polishing procedure into a carbon-free polishing procedure by aims of diamond-free abrasive
- High speed machining could be use as polishing procedure.

In this contribution, the first bullet was tested and demonstrated its efficiency in avoiding the formation of pits after a surface etching of 1.65 μm.

Finally, new cleaning experiments on carbon containing films should be performed in order to investigate the influence of the carbon amount in the Beilby and in the deformed layer on the pit formation. Depending on the ITER final polishing procedure, the carbon amount in the mirrors should be determined prior to the mirrors use in ITER. It involves determining the maximal amount of carbon acceptable for the FMs in order to avoid inducing optical deteriorations after oxygen contamination.

Declaration of Competing Interest

The authors declare that they have no known competing financial interests or personal relationships that could have appeared to influence the work reported in this paper.

CRediT authorship contribution statement

Fabien Sanchez: Writing – original draft, Investigation, Formal analysis, Visualization. **L. Marot:** Investigation, Supervision, Project administration, Funding acquisition, Formal analysis, Writing – review & editing. **R. Steiner:** Investigation, Methodology. **D. Mathys:** Investigation. **P. Hiret:** Investigation. **K. Soni:** Investigation, Writing – review & editing. **R. Antunes:** Investigation, Supervision, Writing – review & editing. **M. Kisiel:** Investigation, Conceptualization. **C. Romero-Muñiz:** Conceptualization, Writing – review & editing. **L. Moser:** Conceptualization, Writing – review & editing. **F. Le Guern:** Conceptualization. **J.J. Piqueras Meseguer:** Conceptualization. **E. Meyer:** Project administration.

Data availability

The raw/processed data required to reproduce these findings cannot be shared at this time as the data also forms part of an ongoing study.

Acknowledgments

This work has been carried out within the framework of the EUROfusion Consortium and has received funding from the Euratom research and training programme 2014–2018 and 2019–2020 under grant agreement No 633053. The views and opinions expressed herein do not necessarily reflect those of the European Commission. The authors would like to thank the Swiss Nanoscience Institute are acknowledged for their financial support. This work was supported by the Swiss State Secretariat for Education, Research and Innovation (SERI) under contract number 22.00424. The work leading to this publication has been funded partially by Fusion for Energy under contracts F4E-OPE-1038 and F4E-OPE-1071. This publication reflects the views only of the author, and Fusion for Energy cannot be held responsible for any use which may be made of the information contained therein.

Supplementary material

Supplementary material associated with this article can be found, in the online version, at 10.1016/j.jnucmat.2023.154382.

References

[1] P. Shigin, N. Babinov, G. De Temmerman, A. Danisi, A. Dmitriev, J. Larsen, R. Madsen, L. Marot, L. Moser, E. Mukhin, et al., RF discharge mirror cleaning system development for iter diagnostics, Fusion Eng. Des. 164 (2021) 112162.

[2] C. Pastor, C. Rodriguez, M. Medrano, A. Soleto, R. Carrasco, F. Lapayese, A. de la Pena, E. Rincon, S. Cabrera, A. Pereira, et al., Optical design of ex-vessel components for the wide angle viewing system diagnostic for ITER, Fusion Eng. Des. 168 (2021) 112607.

[3] L. Marot, C. Linsmeier, B. Eren, L. Moser, R. Steiner, E. Meyer, Can aluminium or magnesium be a surrogate for beryllium: a critical investigation of their chemistry, Fusion Eng. Des. 88 (9–10) (2013) 1718–1721.

[4] L. Moser, R. Steiner, F. Leipold, R. Reichle, L. Marot, E. Meyer, Plasma cleaning of ITER first mirrors in magnetic field, J. Nucl. Mater. 463 (2015) 940–943.

[5] R. Yan, L. Moser, B. Wang, J. Peng, C. Vorpahl, F. Leipold, R. Reichle, R. Ding, J. Chen, L. Mu, et al., Plasma cleaning of ITER edge Thomson scattering mock-up mirror in the EAST tokamak, Nucl. Fusion 58 (2) (2017) 026008.

[6] A.V. Rogov, Y.V. Kapustin, A.G. Alekseev, Application of the penning discharge for cleaning mirrors in optical diagnostics of the ITER, Instrum. Exp. Tech. 58 (1) (2015) 161–166.

[7] P. Jiao, Y. Rong, C. Junling, D. Rui, L.I. Yingying, F. Chong, Study on plasma cleaning of the large-scale first mirror of the charge exchange recombination spectroscopy diagnostic on EAST, Plasma Sci. Technol 22 (3) (2019) 034004.

[8] A. Ushakov, A. Verlaan, R. Ebeling, A. Rijfers, R. O'Neill, M. Smith, B. Stratton, N. Koster, J. van der List, A. Gattuso, et al., Removing W-contaminants in helium and neon RF plasma to maintain the optical performance of the ITER UWAVS first mirror, Fusion Eng. Des. 136 (2018) 431–437.

[9] K. Soni, L. Moser, R. Steiner, D. Mathys, F. Le Guern, J. Piqueras, L. Marot, E. Meyer, Plasma cleaning of steam ingressed ITER first mirrors, Nucl. Mater. Energy 21 (2019) 100702.

[10] A.M. Dmitriev, N.A. Babinov, A.N. Bazhenov, I.M. Bukreev, D.I. Elets, V.V. Filimonov, A.N. Koval, G.S. Kueskiev, A.E. Litvinov, E.E. Mikhin, et al., RF plasma cleaning of water-cooled mirror equipped with notch filter based on shorted λ/4 line, Fusion Eng. Des. 146 (2019) 1390–1393.

[11] A. Litnovsky, P. Wienhold, V. Philipps, G. Sergienko, O. Schmitz, A. Kirschner, A. Kreter, S. Droste, U. Samm, P. Mertens, et al., Diagnostic mirrors for ITER: a material choice and the impact of erosion and deposition on their performance, J. Nucl. Mater. 363 (2007) 1395–1402.

[12] A. Uccello, B. Eren, L. Marot, D. Dellasega, A. Maffini, R. Steiner, D. Mathys, E. Meyer, M. Passoni, Deuterium plasma exposure of rhodium films: role of morphology and crystal structure, J. Nucl. Mater. 446 (1–3) (2014) 106–112.

[13] A. Maffini, L. Moser, L. Marot, R. Steiner, D. Dellasega, A. Uccello, E. Meyer, M. Passoni, In situ cleaning of diagnostic first mirrors: an experimental comparison between plasma and laser cleaning in ITER-relevant conditions, Nucl. Fusion 57 (4) (2017) 046014.

[14] L. Moser, L. Marot, R. Steiner, M. Newman, A. Widdowson, D. Ivanova, J. Likonen, P. Petersson, G. Pintsuk, M. Rubel, et al., Plasma cleaning of beryllium coated mirrors, Phys. Scr. 2016 (T167) (2016) 014069.

[15] L. Moser, R.P. Doerner, M.J. Baldwin, C.P. Lungu, C. Porosnicu, M. Newman, A. Widdowson, E. Alves, G. Pintsuk, J. Likonen, et al., Investigation and plasma cleaning of first mirrors coated with relevant ITER contaminants: beryllium and tungsten, Nucl. Fusion 57 (8) (2017) 086019.

[16] M.B. Yaala, L. Moser, R. Steiner, B. Butoi, P. Dinca, P. Petersson, L. Marot, E. Meyer, Deuterium as a cleaning gas for ITER first mirrors: experimental study on beryllium deposits from laboratory and JET-ILW, Nucl. Fusion 59 (9) (2019) 096027.

[17] K. Soni, L. Moser, C. Porosnicu, R. Antunes, R. Arredondo, P. Dinca, R. Steiner, L. Marot, E. Meyer, Deuterium plasma sputtering of mixed Be-W layers, J. Nucl. Mater. 564 (2022) 153671.

[18] L. Moser, L. Marot, R. Steiner, R. Reichle, F. Leipold, C. Vorpahl, F. Le Guern, U. Walach, S. Alberti, I. Furno, et al., Plasma cleaning of ITER first mirrors, Phys. Scr. 2017 (T170) (2017) 014047.

[19] A. Litnovsky, V.S. Voitsenya, R. Reichle, M. Walsh, A. Razdobarin, A. Dmitriev, N. Babinov, L. Marot, L. Moser, R. Yan, et al., Diagnostic mirrors for ITER: research in the frame of international tokamak physics activity, Nucl. Fusion 59 (6) (2019) 066029.

[20] L. Marot, G. De Temmerman, P. Oelhafen, G. Covarel, A. Litnovsky, Rhodium coated mirrors deposited by magnetron sputtering for fusion applications, Rev. Sci. Instrum. 78 (10) (2007) 103507.

[21] L. Marot, G. De Temmerman, V. Thommen, D. Mathys, P. Oelhafen, Characterization of magnetron sputtered rhodium films for reflective coatings, Surf. Coat. Technol. 202 (13) (2008) 2837–2843.

[22] L. Moser, L. Marot, B. Eren, R. Steiner, D. Mathys, F. Leipold, R. Reichle, E. Meyer, Towards plasma cleaning of ITER first mirrors, Nucl. Fusion 55 (6) (2015) 063020.

[23] L. Moser, Plasma cleaning of diagnostic first mirrors for the nuclear fusion machine ITER, University of Basel, 2017 Ph.D. thesis.

[24] L. Marot, L. Moser, R. Steiner, W. Erni, M. Steinacher, S. Dine, C. Porosnicu, C.P. Lungu, K. Soni, R. Antunes, et al., RF discharge mirror cleaning for iter optical diagnostics using 60 MHz very high frequency, Fusion Eng. Des. 163 (2021) 112140.

[25] J.M. Elson, J.M. Bennett, Calculation of the power spectral density from surface profile data, Appl. Opt. 34 (1) (1995) 201–208.

[26] F.M. Mwema, O.P. Oladijo, T.S. Sathiaraj, E.T. Akinlabi, Atomic force microscopy analysis of surface topography of pure thin aluminum films, Mater. Res. Express 5 (4) (2018) 046416.

[27] Y. Gong, S.T. Misture, P. Gao, N.P. Mellott, Surface roughness measurements using power spectrum density analysis with enhanced spatial correlation length, J. Phys. Chem. C 120 (39) (2016) 22358–22364.

[28] P. Dash, P. Mallick, H. Rath, A. Tripathi, J. Prakash, D.K. Avasthi, S. Mazumder, S. Varma, P.V. Satyam, N.C. Mishra, Surface roughness and power spectral density study of SHI irradiated ultra-thin gold films, Appl. Surf. Sci. 256 (2) (2009) 558–561.

[29] H.E. Bennett, J.O. Porteus, Relation between surface roughness and specular reflectance at normal incidence, J. Opt. Soc. Am. 51 (2) (1961) 123–129.

[30] C.A. Mack, Reducing roughness in extreme ultraviolet lithography, J. Micro/Nanolithography MEMS MOEMS 17 (4) (2018) 041006.

[31] R.M. Bradley, J.M.E. Harper, Theory of ripple topography induced by ion bombardment, J. Vac. Sci. Technol. A Vac.Surf. Films 6 (4) (1988) 2390–2395.

[32] J. Muñoz-García, L. Vázquez, M. Castro, R. Gago, A. Redondo-Cubero, A. Moreno-Barrado, R. Cuerno, Self-organized nanopatterning of silicon surfaces by ion beam sputtering, Mater. Sci. Eng. R Rep. 86 (2014) 1–44.

[33] U. Valbusa, C. Boragno, F.B. De Mongeot, Nanostructuring surfaces by ion sputtering, J. Phys. Condens. Matter 14 (35) (2002) 8153.

[34] S.K. Tan, A.T.S. Wee, Self-organized nanodot formation on InP (100) by argon ion sputtering at normal incidence, J. Vac. Sci. Technol. B Microelectron. Nanometer Struct. Process. Meas.Phenomena 24 (3) (2006) 1444–1448.

[35] B. Ziberi, F. Frost, B. Rauschenbach, T. Höche, Highly ordered self-organized dot patterns on Si surfaces by low-energy ion-beam erosion, Appl. Phys. Lett. 87 (3) (2005) 033113.

[36] A. Molle, F.B. de Mongeot, A. Molinari, F. Xiaerding, C. Boragno, U. Valbusa, Self-organized formation of rhomboidal nanopyramids on fcc (110) metal surfaces, Phys. Rev. Lett. 93 (25) (2004) 256103.

[37] A. Levandovsky, L. Golubović, D. Moldovan, Interfacial states and far-from-equilibrium transitions in the epitaxial growth and erosion on (110) crystal surfaces, Phys. Rev. E 74 (6) (2006) 061601.

[38] A. Molle, A. Toma, C. Boragno, U. Valbusa, F.B. de Mongeot, Nanostructuring Rh(110) surfaces by ion etching, MRS Online Proc. Lib. (OPL) 960 (2006).

[39] A.E. Gorodetsky, R.K. Zalavutdinov, V.L. Bukhovets, A.V. Markin, A.P. Zakharov, T.V. Rybkina, V.I. Zolotarevsky, E.E. Mukhin, A.G. Razdobarin, A.M. Dmitriev, Blistering of mechanically polished molybdenum upon its exposure to deuterium-containing plasma, J. Surf. Invest. X-ray Synchrotron Neutron Tech. 10 (6) (2016) 1214–1225.

[40] A.E. Gorodetsky, A.V. Markin, V.L. Bukhovets, V.L. Voytitsky, T.V. Rybkina, R.K. Zalavutdinov, V.I. Zolotarevsky, A.P. Zakharov, I.A. Arkhipushkin, L.P. Kazansky, et al., Effect of techniques for polishing molybdenum mirrors on their optical stability under cleaning D_2-N_2 plasma, J. Surf. Invest. 14 (5) (2020) 1003–1015.

[41] A.E. Gorodetsky, V.L. Bukhovets, A.V. Markin, V.L. Voytitsky, T.V. Rybkina, R.K. Zalavutdinov, A.P. Zakharov, V.I. Zolotarevsky, I.A. Arkhipushkin, L.P. Kazansky, On the change in the reflectance of Mo(111) mirrors after exposure to D_2-N_2 plasma, J. Surf. Invest. 13 (6) (2019) 1045–1053.

[42] A.E. Gorodetsky, V.L. Bukhovets, R.K. Zalavutdinov, A.V. Markin, L.P. Kazansky, I.A. Arkhipushkin, T.V. Rybkina, A.P. Zakharov, V.L. Voytitsky, E.E. Mukhin, et al., Blistering in molybdenum foils under exposure to the glow discharge of D_2-N_2 mixtures, J. Surf. Invest. 12 (6) (2018) 1052–1060.

[43] A. Litnovsky, 2020. Report of the First Mirror SWG, 38th Meeting of the ITPA TG on Diagnostics.

[44] W.J. Tomlinson, K. Blick, Substrate roughness, cold work and the oxidation of pure iron at 200 to 600 °C, J. Mater. Sci. Lett. 9 (9) (1990) 1005–1010.

[45] A.V. Rogov, Y.V. Kapustin, V.M. Gureev, A.G. Domantovskii, Ion-stimulated pitting during the successive irradiation of molybdenum mirrors with helium and argon ions, J. Surf. Invest. 15 (3) (2021) 563–569.

[46] R. Kelly, N.Q. Lam, The sputtering of oxides Part I: a survey of the experimental results, Radiat. Eff. 19 (1) (1973) 39–48.

[47] P. Sigmund, Theory of sputtering I. Sputtering yield of amorphous and polycrystalline targets, Phys. Rev. 184 (2) (1969) 383.

[48] M.D. Coventry, J.P. Allain, D.N. Ruzic, D^+, He^+ and H^+ sputtering of solid and liquid phase tin, J. Nucl. Mater. 313 (2003) 636–640.

[49] T. Nenadović, B. Perraillon, v. Bogdanov, Z. Djordjević, M. Milić, Sputtering and surface topography of oxides, Nucl. Instrum. Methods Phys. Res. Sect. B 48 (1–4) (1990) 538–543.